

Time and space-correlated plasma potential measurements in the near field of a coaxial Hall plasma discharge

Cite as: Phys. Plasmas **16**, 073504 (2009); <https://doi.org/10.1063/1.3155097>

Submitted: 24 March 2009 . Accepted: 26 May 2009 . Published Online: 16 July 2009

A. W. Smith, and M. A. Cappelli



View Online



Export Citation

ARTICLES YOU MAY BE INTERESTED IN

[Cross-field electron transport induced by a rotating spoke in a cylindrical Hall thruster](#)

Physics of Plasmas **19**, 013503 (2012); <https://doi.org/10.1063/1.3671920>

[Growth of resistive instabilities in \$E \times B\$ plasma discharge simulations](#)

Physics of Plasmas **15**, 012102 (2008); <https://doi.org/10.1063/1.2823033>

[Time-resolved laser-induced fluorescence measurement of ion and neutral dynamics in a Hall thruster during ionization oscillations](#)

Journal of Applied Physics **118**, 233301 (2015); <https://doi.org/10.1063/1.4937272>



NEW!

Sign up for topic alerts
New articles delivered to your inbox

The AIP Publishing logo is located in the bottom right corner of the banner.

Time and space-correlated plasma potential measurements in the near field of a coaxial Hall plasma discharge

A. W. Smith^{1,a)} and M. A. Cappelli²

¹*Department of Mechanical Engineering, Stanford University, Building 520: 521E, Stanford, California 94305-3032, USA*

²*Department of Mechanical Engineering, Stanford University, Building 520: 520D, Stanford, California 94305-3032, USA*

(Received 24 March 2009; accepted 26 May 2009; published online 16 July 2009)

Space- and time-correlated measurements of floating and plasma potential are made in the near field, external flow cathode region of a coaxial Hall plasma discharge using an emissive probe synchronized to quasicohherent fluctuations in discharge current. The luminous axial feature frequently observed in the near field of operating plasma accelerators is found to be concomitant with a spike in the plasma potential (and electron temperature). The structure of the plasma potential allows for multiple avenues for back-streaming ions to accelerate toward the discharge front pole and may pull some classes of ions toward the central axis. The fluctuations in plasma properties exhibit a complex structure at frequencies on the order of the so-called “breathing mode” ionization instability often seen in these types of discharges. Most notably, the plasma potential appears to fluctuate in a helical fashion, resembling tilted drift waves rotating about the central axis. A simple analysis of these waves draws attention to the possible role that they may play in driving anomalous cross-field electron transport in the near field region. © 2009 American Institute of Physics.

[DOI: [10.1063/1.3155097](https://doi.org/10.1063/1.3155097)]

I. INTRODUCTION

Coaxial Hall discharges have been used as high-specific-impulse plasma accelerators for more than 40 yrs.^{1,2} In a typical coaxial Hall plasma accelerator (Fig. 1), the discharge is sustained in imposed orthogonal magnetic and electric fields. The magnetic field magnitude is sufficiently high that the plasma electrons are strongly magnetized and are confined to move predominantly in closed azimuthal $\mathbf{E} \times \mathbf{B}$ drifts, while the plasma ions (usually xenon) are sufficiently massive that they are very weakly confined and move primarily in response to the resulting electric field. As a consequence of the reduced mobility of the electrons along the direction of \mathbf{E} , localized Joule heating efficiently produces ions that are accelerated to high velocities. Ion velocities in excess of 10 km/s are typical,³ depending on the discharge potential established between an external cathode and an anode often positioned at the base of the annular channel.

Within the annular wall-confined channel itself, early studies discovered the existence of axial current beyond that predicted by classical transport.⁴ This “anomalous” cross-field transport of electrons has been the subject of much research. Leading candidates for the source of this anomalous transport are fluctuations in the plasma properties,^{4–6} often modeled using a Bohm conductivity,⁷ and near-wall conductivity resulting from the interaction of electrons with the channel wall.^{8,9} In the near field of Hall plasma accelerators defined to lie between the exit of the annular channel and the external cathode, there are no plasma confining walls and a Bohm model for the electron mobility is often assumed when simulating this region.^{10,11} However, no clear evidence exists which links transport to plasma fluctuations in this region.

A complete understanding of plasma transport within the near field requires a thorough knowledge on the plasma structure. Researchers have conducted numerous experiments to measure the time-averaged electric potential in the near field^{10,12–16} and time-correlated electron temperature and plasma potential measurements have been recorded at a discrete spatial location.¹⁷ In this paper, we carry out similar investigations but expand them to include time- and space-correlated measurements of the floating potential, plasma potential, and electron temperature throughout much of the near field, allowing an unprecedented visualization of the field dynamics. We examine the mean (time-averaged) and low-frequency structure of these properties within a Hall discharge accelerator that operates at relatively low power.¹⁸ The results of our comprehensive set of emissive probe measurements show that these properties fluctuate significantly (in particular, the plasma potential and electron temperature), revealing the presence of an azimuthal drift wave that may be coupled or strongly interacting with the so-called breathing mode ionization instability that is characteristic of these types of discharges.^{19,20} As described below, this complex time-dependent structure may impact electron transport properties possibly accounting for the current flow in this region.

II. EXPERIMENTS

The coaxial Hall plasma accelerator studied here is a variation in a low power (nominally 200 W) discharge of the type described in the prior literature.¹⁸ It has a coaxial channel of ~ 20 mm in length, 8 mm in width, and a mean channel radius of $r_m = 11.7$ mm. The discharge was operated in voltage-limited mode with a voltage and current of 200 V and 800 mA, respectively. The magnetic field peaks near the

^{a)}Electronic mail: awsmith@stanford.edu.

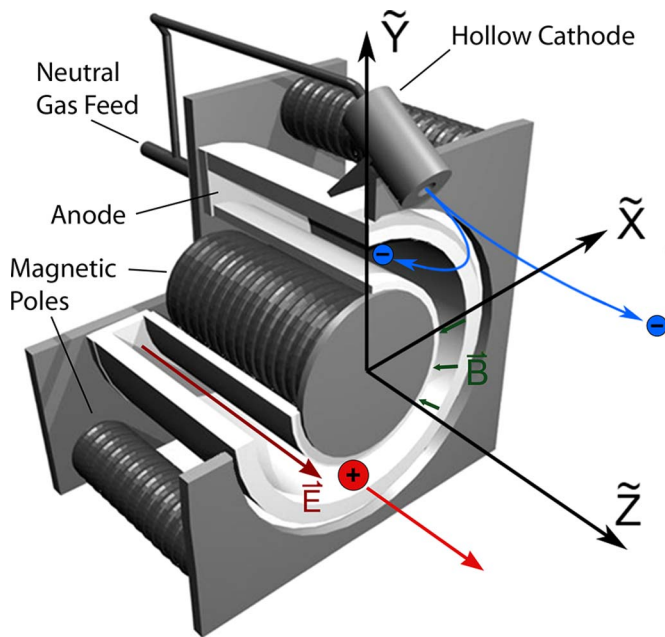


FIG. 1. (Color online) Schematic of a typical coaxial Hall thruster.

exit plane at a value of about 0.05 T. The cathode keeper was maintained at 14 V and 500 mA, respectively, with 3 A of current through the heater. Argon was used as the cathode gas with a flow rate of 2 SCCM (SCCM denotes cubic centimeter per minute at STP) and xenon was used as the primary discharge gas with a flow of 8.5 SCCM through the channel.

The time-dependent discharge current is measured by monitoring the voltage across a shunt resistor (1.0Ω) at the anode side of the circuit using a differential voltage probe. Strong periodic fluctuations in the anode current are seen due to the breathing mode ionization instability which creates macroscopic fluctuations in plasma properties within the discharge and near field.²⁰ The discharge is operated in a vacuum facility consisting of a stainless-steel chamber of 1.25 m in diameter and 4 m long. The base pressure in the facility during thruster operation is 1.2×10^{-5} Torr.

The potential distribution throughout the near field of the discharge was measured using a floating emissive probe similar to that described by Haas and Gallimore.²¹ An excellent overview of plasma diagnostics including emissive probes is presented by Hershkowitz.²² The emitting portion of the probe consists of a 2 mm diameter loop of $150 \mu\text{m}$ diameter thoriated-tungsten (1%) wire. The loop is oriented so that the normal to the plane formed by the loop is parallel to the x -direction, as shown in Fig. 1. The ends of this filament are mechanically crimped to copper wire and inserted into parallel holes in a 2.5 mm diameter alumina tube. The ends of the alumina tube are then sealed with an alumina paste. The photograph of the probe in Fig. 2 has the filament partially withdrawn from the alumina insulator and the insulating paste has not yet been applied. Alternating current is driven through the probe and coupled through an isolation transformer so that its floating potential can be recorded on a digital oscilloscope. While other researchers have experienced problems with melting of the copper wires,²³ we have

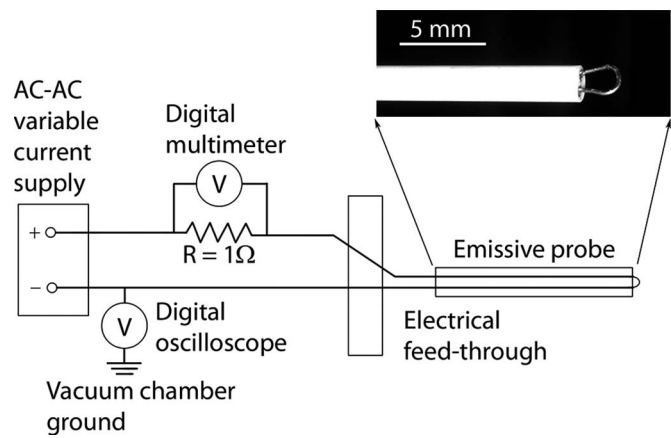


FIG. 2. Schematic of emissive probe circuit.

found that our construction allows for probe lifetimes on the order of 2–4 h, and the typical failure mode is evaporative mass loss in the filament itself.

The basic theory of emissive probe characteristics is reasonably well established.^{22,24} A thermionic electron-emitting filament in a low-temperature plasma will float at a potential which approaches the plasma potential when the emitted electron current is sufficiently high (i.e., the filament is sufficiently heated) to neutralize the plasma sheath. Figure 3 shows a typical set of measurements of the floating potential versus applied (rms) heating current ranging from an unheated state through probe failure. The approximate color of the filament is labeled in the figure along with an estimate of the filament temperature.²⁵ As is commonly seen in practice, the floating potential of the probe never truly saturates but instead levels off as the heating current is increased (in the case of Fig. 3, this occurs for heating currents in excess of about 2 A). Dorf *et al.*²⁶ present a detailed analysis of uncertainties in emissive probe plasma potential measurements and show that for a xenon plasma $\phi_{\text{pl}} = \phi_h + 1.5T_e - \Delta\phi^*$, where ϕ_{pl} is the true plasma potential, ϕ_h is the measured floating potential of the emissive probe in the heated state, T_e is the electron temperature, and $\Delta\phi^* = \ln[(4.5j_{\text{em}})/j_e^{\text{sat}}]T_{\text{pr}}/e$ with j_{em} being the current density of emitted electrons that reach the plasma, j_e^{sat} is the electron saturation current den-

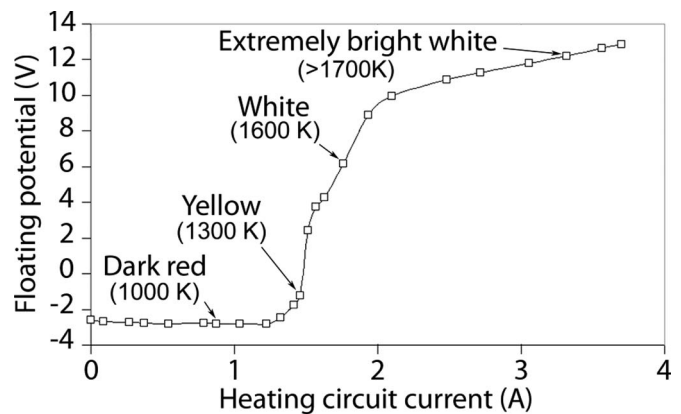


FIG. 3. Floating voltage vs heating current for an emissive probe (labels denote the approximate color and temperature of filament).

sity, T_{pr} is the probe temperature, and e is the electron charge. Following Ref. 26 for a thoriated-tungsten filament at 2000 K, $j_{em} \approx 2.5$ A/cm². For the thruster in the current study, j_e^{sat} ranges from $O(10^{-1}$ A/cm²) near the exit plane to $O(10^{-2}$ A/cm²) further from the channel, so $\Delta\phi^*$ ranges from 0.82 V near the exit plane to 1.21 V further from the channel. While the trace in Fig. 3 is representative of the traces obtained throughout the near field, in regions of the plasma where the probe is strongly heated by the plasma, the current needed to approach the saturated state is considerably lower. In fact, if left stationary in such regions, the probe can be made to be self-emitting even without external heating. Since there is no clear saturation of the probe, we have defined the measured plasma potential as the probe floating potential measured when it is heated with a current of 3.25 A. While this introduces a systematic uncertainty in the extracted plasma potential (underestimating the true plasma potential by several volts), it is considered to be a reasonable tradeoff as it allows us to rapidly acquire the potential by translating the probe over three-dimensional space while at a constant probe heater current. A survey of the probe response at a number of spatial locations indicates that a current of 3.25 A is sufficiently high to be in the saturation branch at all points in the near field studied here, while still low enough to avoid dramatically shortening the lifetime of the probe. The discharge current was monitored during the tests and the average current was found to vary by less than 1.5% for all of the points tested, regardless of the probe position relative to the thruster. In this sense, any perturbations introduced by the probe were relatively small.

The unheated (floating) potential is mapped throughout the near field, taking care to rapidly move the probe in and out of regions of strong heating (such as very near the exit plane) so that it does not become self-emitting. Three translation stages are oriented to allow a relative motion between the probe and thruster in three orthogonal directions. The thruster is mounted on a pair which allows for translational speeds of 1–3 cm/s and the probe itself is mounted on a third stage. We use the same positioning algorithm for both the floating and plasma potential measurements and a computer controls both the translation stages and data acquisition on a digital oscilloscope. At each measurement location, the probe is paused for 1 s (to allow any small residual vibrations induced by the translation stages to dampen out), after which the oscilloscope records 50 000 temporal measurements of the probe signal and discharge current simultaneously. These transient measurements are recorded at 8 ns interval (spanning of 400 μ s). After the near-field floating potential measurements are complete, the probe current is raised to 3.25 A and the measurements are repeated to obtain the plasma potential. An example trace of a typical heated probe signal and discharge current is shown in Fig. 4. The inset shows the zero-mean cross correlation of the two signals, indicating that there is a strong correlation between the probe signal and discharge current, and that the probe signal lags the discharge current by 7.5 μ s. An analysis of the power spectrum of the discharge current signal indicates a single peak between 22 and 29 kHz with all other frequency components having magnitudes less than 10^{-3} times that of the low-

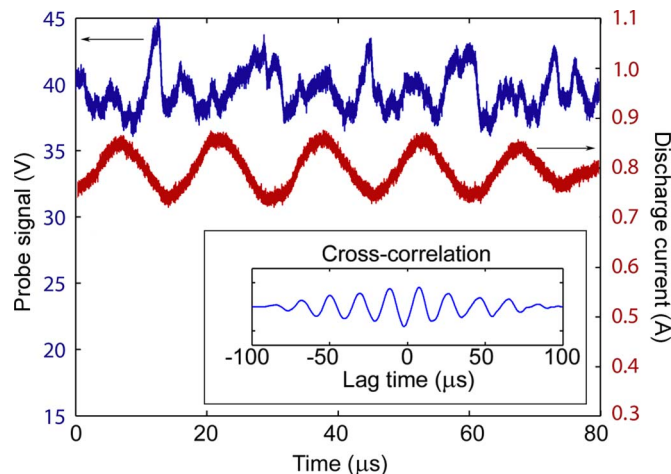


FIG. 4. (Color online) Representative traces of heated probe signal and discharge current (the inset shows the zero-mean cross correlation of the signals).

frequency peak. An analysis of the probe signal shows a single broad peak between 25 and 100 kHz with the higher end of this range having comparable frequency to transit-time instabilities.²⁰ Determining the electron temperature T_e from the floating potential measured by the probe when cold and when heated requires a model of the collected electron and ion current. The theory for ion current collection depends on the relative size of the Debye length λ_D and probe radius r_p . In our case, with typical plasma conditions of $n_e \lesssim 5 \times 10^{11}$ cm⁻³ and $T_e \lesssim 20$ eV, the Debye length is about 50 μ m and $r_p/\lambda_D \sim 1$, and so the ion collection is orbital motion limited. An exact theory for relating the floating potential of an emissive probe to the plasma potential under these conditions is not available. However, a comparison with the theory for planar probes by Raitses *et al.*²⁷ leads to a lower bound and upper bound on the electron temperature

$$0.815\tilde{T}_e \leq T_e \leq 1.142\tilde{T}_e, \quad (1)$$

where \tilde{T}_e is the electron temperature calculated assuming that ions enter the sheath at the Bohm velocity⁷

$$\tilde{T}_e = \frac{2e(\phi_{pl} - \phi_c)}{k \ln(m_i/2\pi m_e)}. \quad (2)$$

Here m_i is the mass of the ions (in this case, xenon), m_e is the electron mass, and ϕ_c is the potential measured by the probe in the unheated cold state. For the purposes of the results which follow, we have taken $T_e = \tilde{T}_e$ assuming $\phi_{pl} = \phi_h$, implying an uncertainty of at least $\pm 17\%$ on the measured temperature attributable alone to the uncertainty in ion collection models. In reality, the true electron temperature is expected to tend toward the higher end of the range due to the underestimation of the plasma potential.

III. RESULTS AND ANALYSIS

Results presented here are for spatial variables nondimensionalized by the mean channel radius r_m . That is, $\tilde{X} = x/r_m$, $\tilde{Y} = y/r_m$, and $\tilde{Z} = z/r_m$. The coordinate convention is that shown in Fig. 1. We take $z=0$ to be the exit plane and

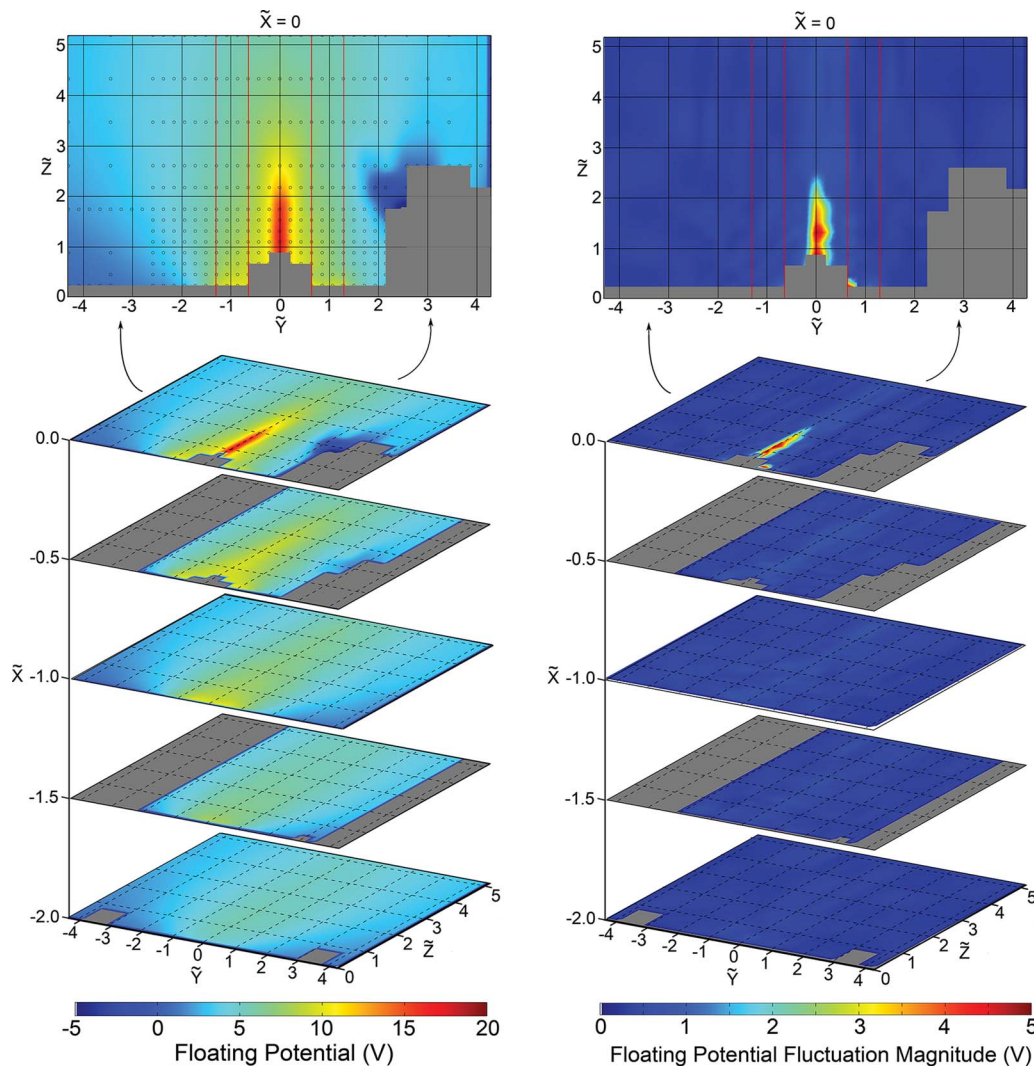


FIG. 5. (Color online) Spatial slices of the measured floating potential (left) and the magnitude of the floating potential fluctuations (right).

$(x, y, z) = (0, 0, z)$ to define the central axis of the thruster. In all cases, the cathode and chamber ground are assigned at 0 V. Regions where no measurements were made are indicated by filled gray or white areas. The measurements were stopped (at $z = 0.2r_m$) just short of the exit plane to avoid a possible contact between the thruster and the probe when the translation stages were in motion. Other features of the thruster (the shape of the inner insulator as well as the cathode location) also precluded the probing of certain regions of the near field.

The mean (time-averaged) properties calculated from the transient probe traces were interpolated to a discretization of $0.10r_m$ and plotted in the left panels of Figs. 5–7. In the $x=0$ plane of the floating and plasma potential plots, the positions where probe measurements were obtained are indicated by open black circles and the channel boundaries are indicated by red lines extending along z (the channel exists for $z < 0$). The channel spans a radial distance between $0.65r_m$ and $1.35r_m$ (from $y = 0.65r_m$ to $1.53r_m$ in the $x=0$ plane). The measurement points and channel boundaries are not shown in the other planes for clarity. The measurement locations were nearly identical in the other x -planes; however, the

greatest concentration of measurements was near the center of the thruster and along the central axis where the gradients in the potential were significant.

The time-averaged floating potential (left panel of Fig. 5) shows a prominent spike along the centerline of the thruster, reaching a maximum of 18 V near $z = 1.2r_m$ before gradually diminishing to 7 V at $z = 5r_m$. This potential spike diminishes more rapidly along x and y . The floating potential near the channel exit is also elevated, although nowhere does the floating potential exceed 11 V except along the central axis. Moving away from the central axis and exit plane of the thruster, the floating potential gradually decreases to a value between 3 and 6 V. The region of the plasma nearest to the cathode [which is located at $(x, y, z) = (0, 2.6r_m, 1.75r_m)$] is characterized by a strong depression of the floating potential falling below -5 V. With the exception of this region, the floating potential is highly axisymmetric.

The magnitude of the floating potential fluctuations (i.e., the standard deviation in the floating potential temporal traces) peaks at 5 V along the central axis near $z = 1.5r_m$ (see Fig. 5, right panel). The overall structure mimics the structure seen in the floating potential although it is slightly less

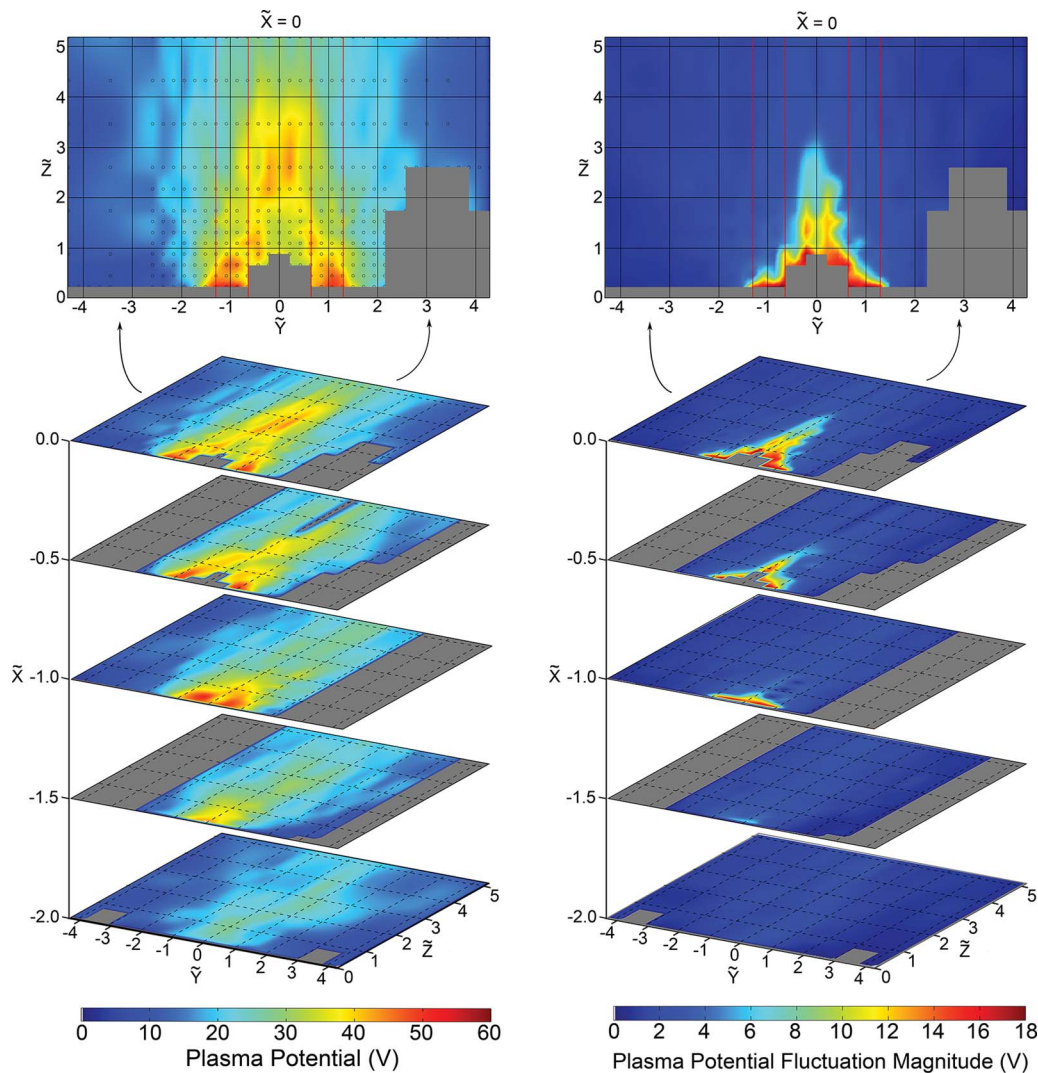


FIG. 6. (Color online) Spatial slices of the measured plasma potential (left) and the magnitude of the plasma potential fluctuations (right).

symmetric (with larger fluctuations present on the cathode side of the central axis).

The plasma potential is less axisymmetric than the floating potential with a much more complex structure. The time-averaged plasma potential shows broad regions of elevated potential over the channel of the thruster which extend far into the near field along the central axis (see Fig. 6). In contrast to the floating potential measurements, the peak plasma potential (58 V) was measured over the channel of the thruster. The potential along the central axis peaks at 45 V near $z=2.75r_m$ and remains elevated (35 V) at $z=4r_m$. The plasma potential gradient is considerably greater parallel to the exit plane than parallel to the central axis with the plasma potential diminishing to less than 10 V within $3r_m$ and $4r_m$ of the central axis. Moving away from the central axis in the x - and y -directions, the presence of the central spike rapidly diminishes (disappearing by $x=r_m$) indicating its narrow three-dimensional beam shape. A depression in the plasma potential exists near the central axis for $z \leq 1.6r_m$ where the potential falls below 30 V. Surrounding this depression are regions where the plasma potential is nearly 50% greater. The upper axial boundary of this depression, which marks

the transition to the elevated potential spike along the axis, corresponds to the spatial location of the onset of the drop in floating potential. The elevated potential along the central axis is actually split by a thin lower-potential valley located immediately along the central axis extending only at $0.1r_m$ to either side of $x, y=0$.

The right panel of Fig. 6 shows the standard deviation of the plasma potential temporal traces which also exhibits a split peak along the central axis. The fluctuations are most intense in the central portion of the near field of the thruster (reaching 18 V); however, they rapidly diminish for $z > 2r_m$. In general, the overall structure mimics the structure seen in the plasma floating potential with the exception of the region along the central axis for $z < 1.6r_m$, where the plasma potential exhibits a depression. Here, the plasma potential fluctuations are actually quite large in places reaching 50% of the mean value.

With the plasma and floating potential mapped out, we can determine the spatial distribution in electron temperature using Eq. (2), taking account of the uncertainty given by Eq. (1). We have chosen to take the center of the range with

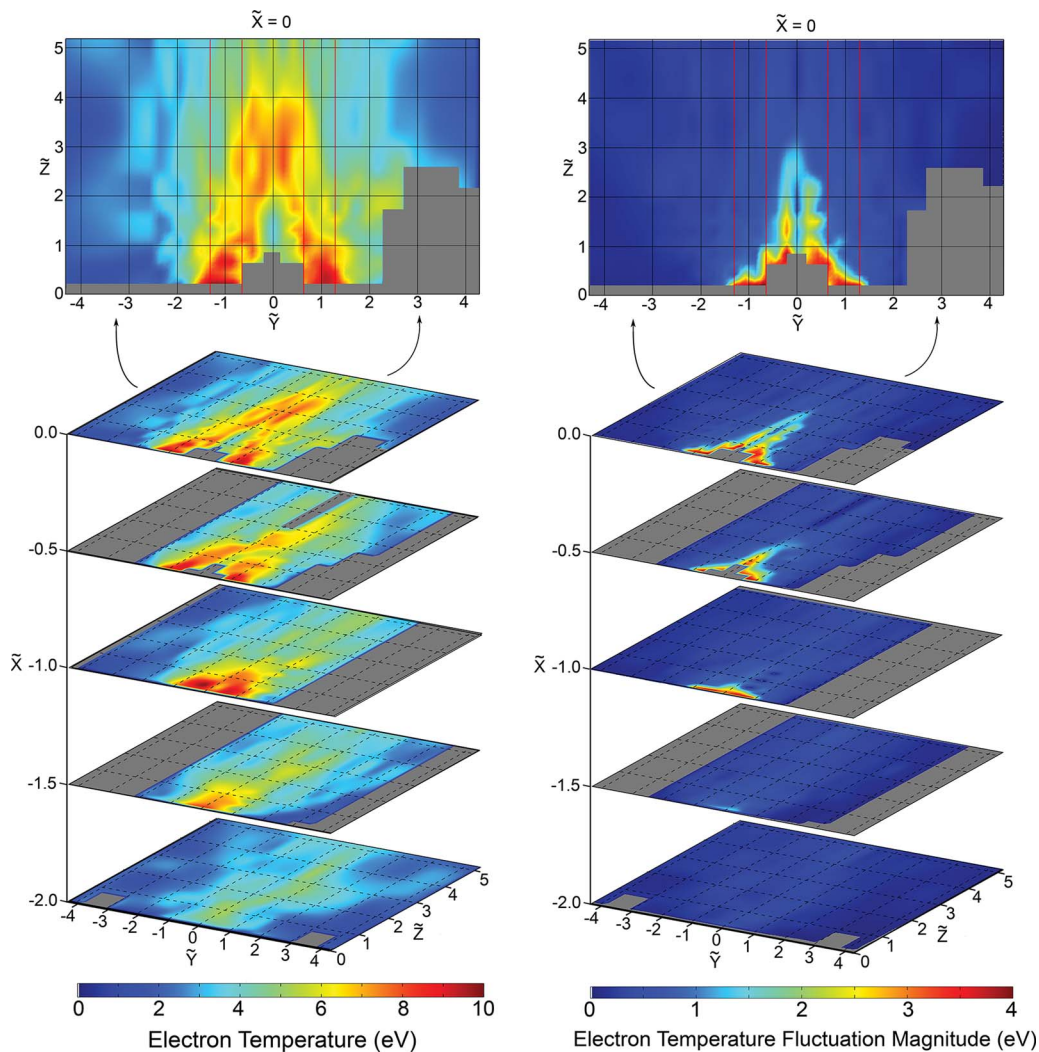


FIG. 7. (Color online) Spatial slices of the inferred electron temperature (left) and the magnitude of the electron temperature fluctuations (right).

$T_e = \tilde{T}_e$ given by Eq. (2). The resulting time-averaged electron temperature is shown in the left panel of Fig. 7. The electron temperature reaches a peak of 10 eV directly over the channel of the thruster. Near the central axis, broad regions of elevated electron temperature extend out to and beyond $z = 4r_m$. This central region of elevated electron temperature is separated by a narrow and shallow valley of lower temperature similar in form to the plasma potential. A much stronger depression in the electron temperature exists along the central axis for $z \lesssim 2r_m$ where it reaches a minimum of 3 eV. This depression is surrounded by nearly continuous ridges of elevated electron temperature (> 7 eV) which link the near-channel regions to the high-temperature spike along the axis at $z \gtrsim 2r_m$. Elsewhere, the electron temperature diminishes to $\lesssim 5$ eV and becomes somewhat more uniform.

The electron temperature fluctuates by more than 4 eV in the regions nearest the channel exit, as shown in the right panel of Fig. 7. As was noted previously for the plasma and floating potentials, the fluctuation magnitude is greatest where the mean electron temperature is highest; however, in the region of $z > 2r_m$ along the central axis, the electron temperature shows significantly smaller fluctuations than would

be expected from this correlation. The fluctuations rapidly diminish for x , y , or $z > 1r_m$ (except along the central axis).

A. Time-correlated results

By simultaneously measuring both the discharge current and probe signals, we can reconstruct the time-correlated plasma potential, floating potential, and electron temperature throughout the near field by synchronizing the temporal data to discharge current fluctuations, which are often attributed to the breathing mode.²⁰ This approach is the same as that taken by Albarede *et al.*¹⁷ in their investigation of low-frequency electron dynamics in the near field of a Hall thruster. The frequency of this breathing mode oscillation is expected to be governed by the residence time of neutral atoms in the acceleration region of the thruster. A reasonable estimate of the neutral xenon velocity is $\sim 1.7 \times 10^4$ cm/s, i.e., about the sonic velocity at room temperature. The acceleration zone is estimated to be around 0.5–1.0 cm long, so we expect the breathing mode frequency to be on the order of 20–30 kHz, a value confirmed by measurements made on a similar thruster by Hargus and Pote.²⁸

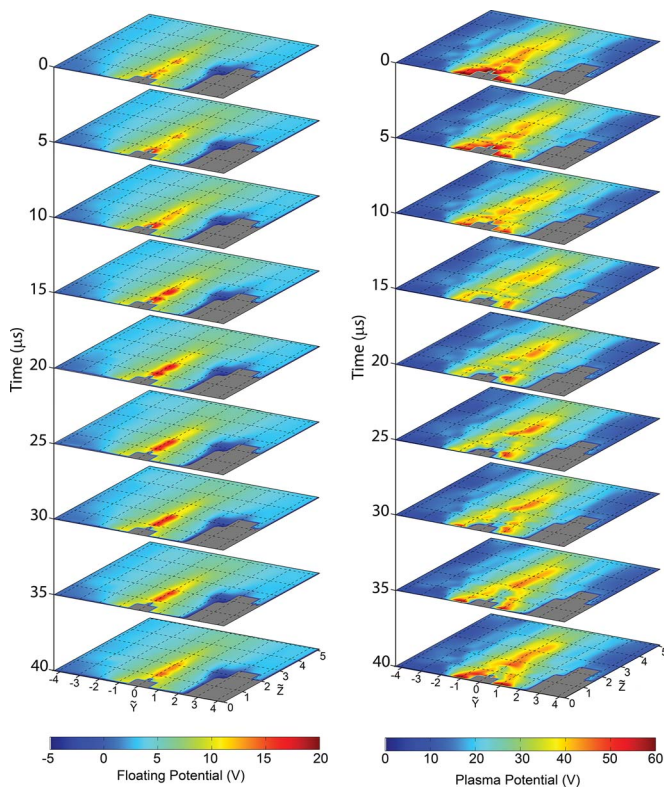


FIG. 8. (Color online) Temporal snapshots of the floating potential (left) and plasma potential (right) in the $x=0$ plane.

In postprocessing the data, we survey the discharge current traces at each spatial location and take the first breathing-mode peak in the discharge current to be $t=0$ (i.e., the initial time) for the given spatial point (see Fig. 4). We repeat this process over all of the measurement locations to synchronize the measurements based on an initial peak in the breathing mode. This method cannot give an absolute determination of the temporal field structure for two primary reasons. First, the measurements were all recorded at separate moments in time, and although the thruster was in a steady-state operation, the discharge properties are not identical from one breathing mode to the next. However, the variability in the mean discharge current was small and the consistency of neighboring measurements (which were not recorded sequentially due to the motion algorithm used to scan the measurement volume) reinforces the validity of our method. Second, the determination of a breathing mode peak is not absolute given the many higher-frequency oscillations present in the signals (see Fig. 4). We estimate that the zero datum ($t=0$) may vary by as much as 5–10 μs due to the higher-frequency oscillations that blur the breathing mode oscillations. This error is nonsystematic (sometimes causing an early start point and sometimes a late start point), however, and we expect that these errors may cancel when viewed over many points.

Figures 8 and 10 show the measured plasma properties in the $x=0$ plane at representative time synchronizations encompassing a range of 40 μs with 5 μs interval and Fig. 9 shows the plasma potential in the $z=0.4r_m$ plane at six representative times spanning at 25 μs . This range of time was

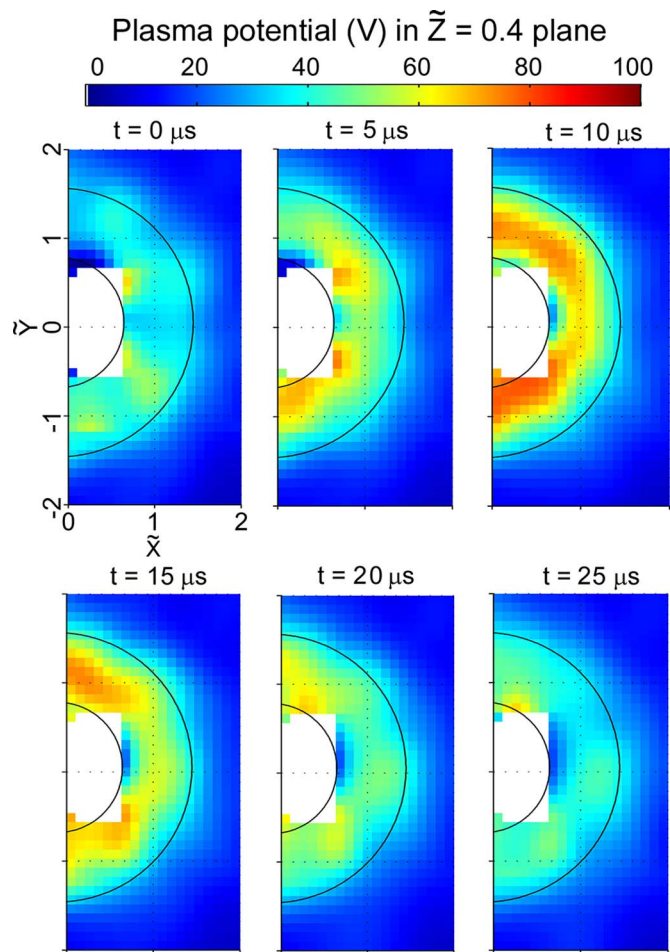


FIG. 9. (Color online) Temporal snapshots of the plasma potential in the $z=0.4r_m$ plane.

chosen because it is approximately the duration of one breathing mode oscillation and the primary fluctuations present in the near field appear to oscillate at this rate. Figures 8–10 are also synchronized to each other with $t=0$ the same for each figure. This allows for a visualization of the simultaneous variation in the floating potential, plasma potential, and electron temperature. In addition to the static figures below, video visualizations that span several breathing mode oscillations have been prepared which more dramatically showcase the transient behavior of the floating potential (Fig. 11), plasma potential (Figs. 12 and 13), and electron temperature (Fig. 14). The videos are available in the online supplement to this paper.

The temporal fluctuation in floating potential (see Fig. 8, left panel) is not as strong as the fluctuation in the plasma potential and electron temperature. The most dominant transient feature is an axial oscillation of the elevated potential region along the central axis. In the figure, the image at $t=0$ shows two regions of elevated potential along the central axis: the first at $0.75r_m < z < 1.5r_m$ and the second at $2r_m < z < 2.5r_m$. The peak potential in both of these regions is ~ 13 V with the intermediate region dropping to around 10 V. In subsequent snapshots, the potential in both regions increases and the features merge into a single axially elongated region of elevated potential spanning at $0.75r_m < z$

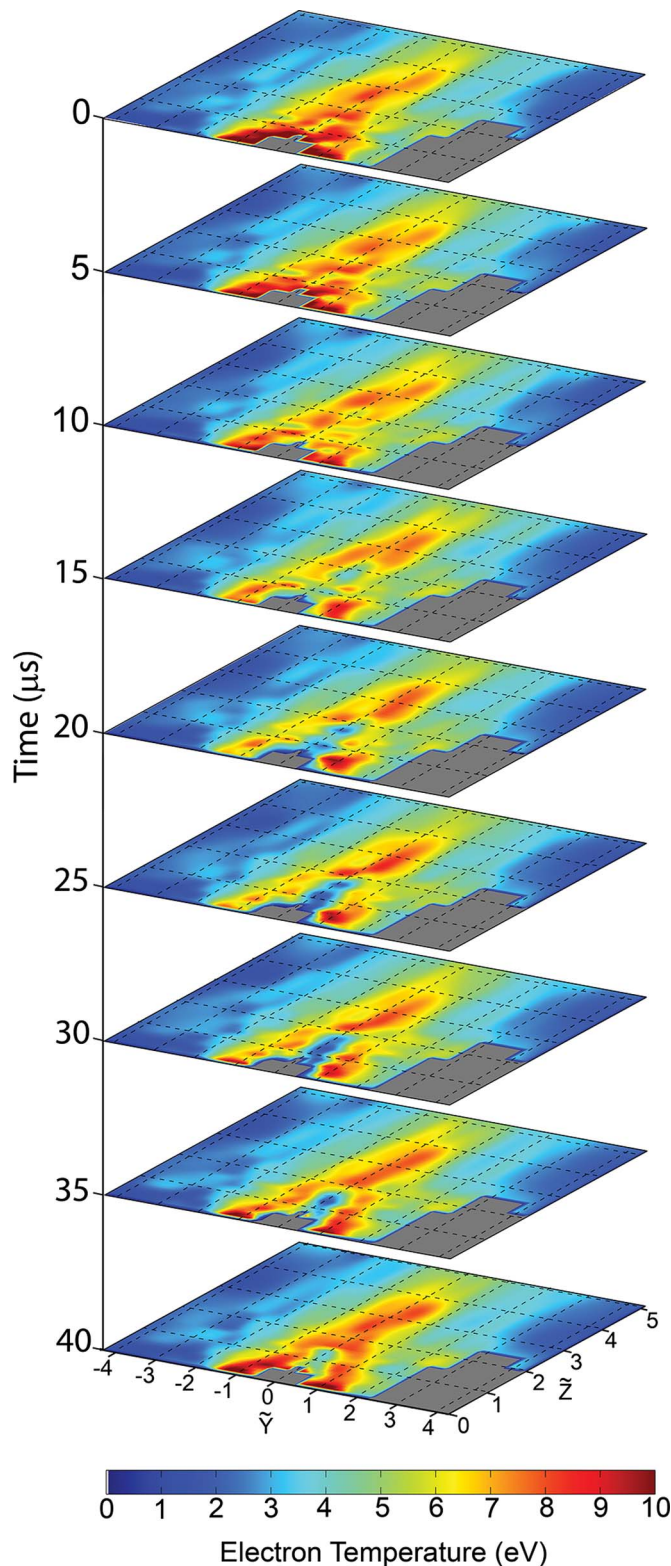


FIG. 10. (Color online) Temporal snapshots of the inferred electron temperature in the $x=0$ plane.

$< 2r_m$. The process repeats at the breathing mode frequency (~ 25 kHz). Other oscillations are present, most notably a subtle bulk oscillation in the magnitude of the floating potential throughout the near field.

In contrast to the floating potential, the plasma potential is highly dynamic and shows a complex transient behavior,

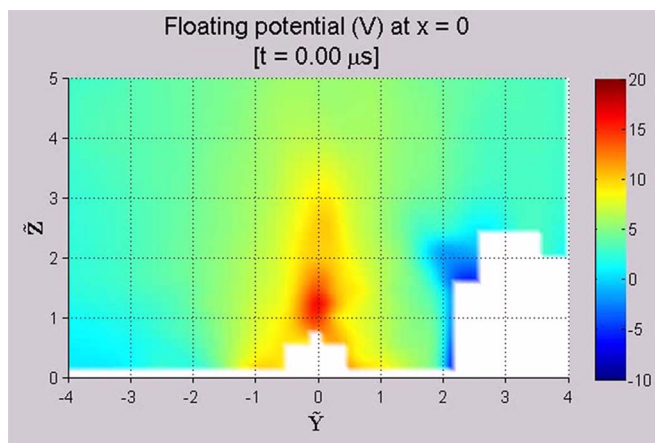


FIG. 11. (Color online) Video clip showing a transient floating potential in the $x=0$ plane (enhanced online). [URL: <http://dx.doi.org/10.1063/1.3155097.1>]

as shown in the right panel of Fig. 8. At first glance, the plasma potential appears to be turbulent; however, a closer inspection reveals subtle patterns in the fluctuations. The most dramatic transient feature is an apparent azimuthal rotation of the regions of elevated plasma potential about the central axis (better shown in Fig. 9). In the first image at $t=0$, there is a broad region of high potential (exceeding 55 V) extending over the central portion of the thruster both over the channels and near the central axis for $z < 1r_m$. The central peak in potential along the axis is not split (as the time-averaged results indicated); rather it is slightly shifted away from the axis toward the positive values of y . By $t=15 \mu s$, the peak potential drops to 45 V, and the region of elevated potential near the axis has started to separate from the regions over the channels and is more strongly shifted toward the positive values of y . At $t=20$ and $25 \mu s$, the plasma potential located over the portion of the channel centered at $y=r_m$ is intensifying while the potential over the opposing portion of the channel (centered at $y=-r_m$) is diminishing. The plasma potential along the central axis for $z < 2r_m$ starts falling at this time dropping below 20 V. At the same time,

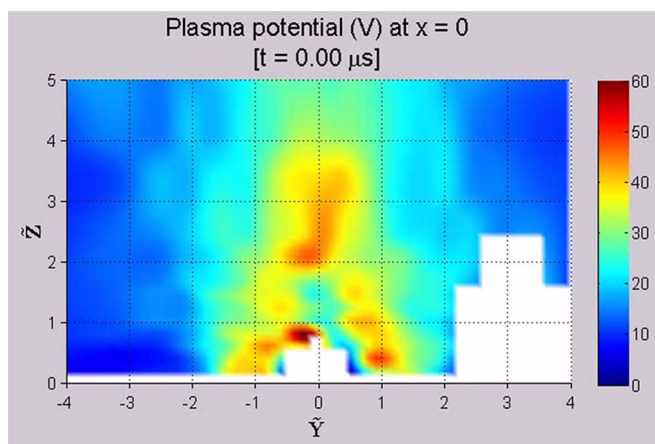


FIG. 12. (Color online) Video clip showing a transient plasma potential in the $x=0$ plane (enhanced online). [URL: <http://dx.doi.org/10.1063/1.3155097.2>]

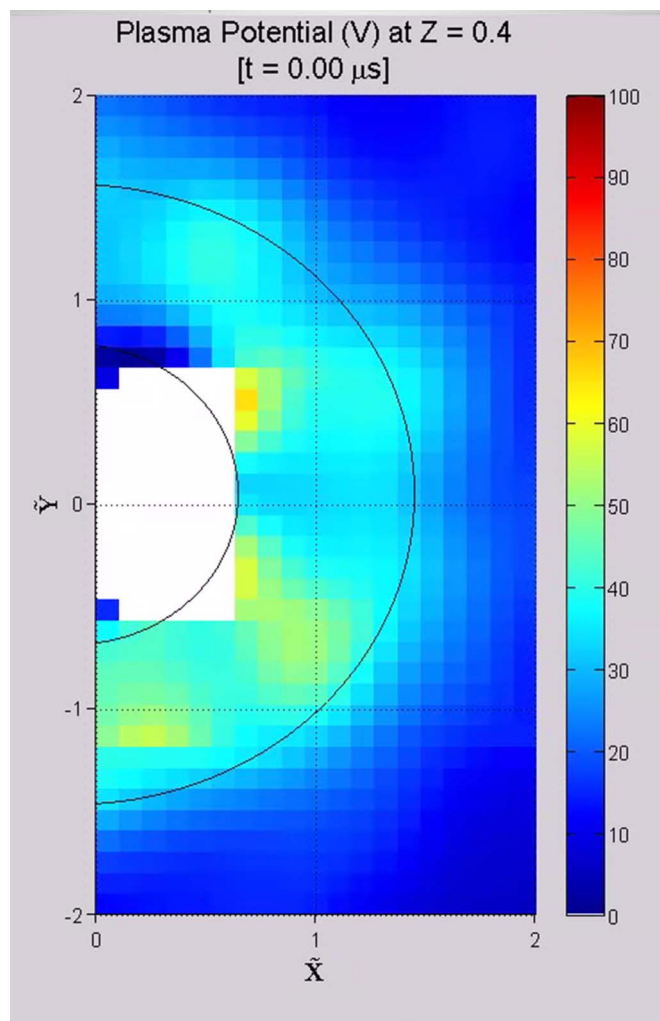


FIG. 13. (Color online) Video clip showing a transient plasma potential in the $z=0.4r_m$ plane (enhanced online). [URL: <http://dx.doi.org/10.1063/1.3155097.3>]

the downstream peak in potential increases in magnitude for $y > 0$. In the final frames, the elevated plasma potential over the channel centered at $y = -r_m$ returns. This sequence of events repeats over time with a frequency close to the breathing mode.

Further details into the character of the fluctuations can be obtained by examining the results in a spatial plane parallel to the exit plane. Figure 9 shows the plasma potential in the $z=0.4r_m$ plane (i.e., just beyond the exit plane) with the channel boundaries indicated with black semicircles (measurements were only obtained for $x > 0$). In this series of images, a region of elevated plasma potential rotates azimuthally in a counterclockwise direction which is opposite the general $\mathbf{E} \times \mathbf{B}$ direction, consistent perhaps with density-gradient driven drift waves. This fluctuation repeats at ~ 25 kHz, indicating an azimuthal velocity of ~ 1800 m/s. The fluctuation appears to be a single wave which rotates about the channel with a wave number of ~ 14 m $^{-1}$. The velocity is approximately four times the azimuthal velocity reported by Hargus and Charles²⁹ and seven times the value reported by Manzella,³⁰ which is not surprising considering

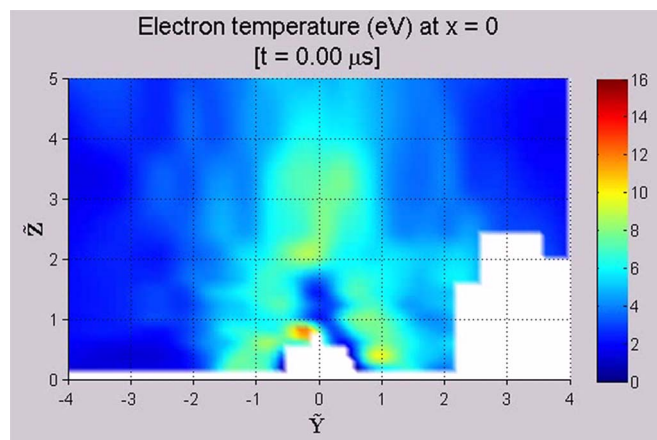


FIG. 14. (Color online) Video clip showing a transient electron temperature in the $x=0$ plane (enhanced online). [URL: <http://dx.doi.org/10.1063/1.3155097.4>]

that different thrusters are involved and that while our measurements track the plasma potential, those of Refs. 29 and 30 are tracking the ions themselves.

As expected, the electron temperature (see Fig. 10) shows the same qualitative dynamical behavior as the plasma potential since the floating potential was found to be fairly quiescent. However, the effect of the axially oscillating floating potential spike along the centerline manifests itself as an oscillation in the electron temperature along the central axis between ~ 1 and ~ 7 eV at $z=r_m$. At $t=0$, there is a broad region of elevated electron temperature extending between $-2r_m < y < 2r_m$ and $z < 5r_m$. This region is more or less continuous with small pockets of locally reduced electron temperature, most notably near $y=0$ for $z < 1.5r_m$. In subsequent frames, the continuous region of elevated electron temperature breaks up and a deep depression in the electron temperature forms along the central axis near the thruster for $z < 2r_m$. A sharp discontinuity in electron temperature develops near $z=2r_m$ for times between $t=15$ μ s and $t=35$ μ s. The electron temperature in this depression drops below 1 eV before the depression starts to merge with the surrounding elevated electron temperature regions. The regions of elevated electron temperature mimic the temporal behavior of the plasma potential and oscillate in a twisting (helical) motion about the central axis.

IV. DISCUSSION AND SUMMARY

We have found that the distributions in the floating potential, plasma potential, and electron temperature are highly structured, and, in the case of the plasma potential and electron temperature, are highly variable in time. The time-averaged floating potential shows a strongly elevated beam-like region along the central axis of the thruster extending more than two mean channel radii away from the exit plane. The floating potential reaches a maximum of 18 V in this region, while over the channels it peaks near 11 V. The central spike is tightly bound to the central axis, diminishing completely within $1r_m$ in the x - and y -directions while extending to $z=3r_m$. The presence of the cathode manifests

itself as a deep depression in the potential (< -5 V). On the whole, the overall floating potential distribution is quite axisymmetric.

The plasma potential exhibits a considerable amount of structure with regions of elevated potential over the channels (which exceed 55 V) and steep broad ridges of high potential connecting to a central split peak along the centerline for $z \gtrsim 1.6r_m$. The elevated potential along the centerline persists for nearly $4r_m$ from the exit plane. Our measurements show that there is a depression in the plasma potential along the central axis for $z \lesssim 2r_m$ in which the plasma potential falls to ~ 30 V surrounded by regions where the plasma potential reaches 40–45 V. This structure allows for the acceleration of back-streaming ions toward the thruster which may be responsible for some of the lifetime-limiting erosion of the insulator materials near the exit plane and in particular on the central pole of Hall thrusters. If a low-energy ion exists near $z \sim 2r_m$ along the central axis (perhaps created via a charge-exchange collision), it will be accelerated toward the thruster. Furthermore, low-energy ions exiting the thruster close to the inner edge of the channel will be drawn toward the central axis.

The electron temperature is elevated over the channel and along the central axis with connecting ridges between the two and it exhibits a strong depression along the axis for $z \lesssim 2r_m$ where the temperature falls to 3 eV. Bordering this depression, steep gradients in the electron temperature (in the $\pm x$ -, $\pm y$ -, and $\pm z$ -directions) lead to surrounding regions in which the electron temperature exceeds 7 and 8 eV.

The results illustrate that the transient plasma potential structure is complex with many fluctuations occurring throughout the near field. The dominant fluctuation in the floating potential is an axial oscillation along the central axis in which two separated regions of elevated potential converge and combine before subsequently splitting and rebounding. The dominant fluctuation in the plasma potential is an azimuthal oscillation over the channel and along the central axis. In addition to this azimuthal oscillation, we find many elevated regions of plasma potential which connect the channel region to the broad spike in plasma potential located along the central axis and oscillate back and forth. The electron temperature generally follows the plasma potential in terms of the fluctuation structure; however, there is an additional oscillation along the central axis for $z \lesssim 2r_m$ where the electron temperature oscillates between very low and more moderate values.

Both the electron temperature and plasma potential are expected to be underestimated (see Sec. II). Given the range of electron temperature measured, the plasma potential is expected to be underestimated by as much as 15 V near the exit plane and 4 V at the outer extent of the experiment domain.

All three of the plasma properties show a distinct transition along the axis near $z = 2r_m$. In the floating potential, the prominent spike in potential along the axis sharply diminishes for $z > 2r_m$. A broad depression in the plasma potential extends along the central axis up to $z \sim 2r_m$, at which point the plasma potential quickly rises to > 45 V. This transition is manifested most clearly in the electron temperature which,

at some instants in time, rises from a low along the axis of < 1 eV at $z \sim 1.9r_m$ to > 8 eV at $z \sim 2r_m$ (see Fig. 10, $t = 25, 30 \mu\text{s}$). To our knowledge, there is no explanation for the location of this transition in the literature and this feature will be studied further in future research.

The nature of the apparent structure of the plasma potential and electron temperature fluctuations is well explained if a twisting helical disturbance is present in the near-field potential. This twisting mode may be due to coupling of the breathing mode oscillation²⁰ and low-frequency azimuthal ($\mathbf{E} \times \mathbf{B}$) oscillations⁴ related to either the ionization process or to density gradient-driven drift wave instabilities.²⁰ In an early study, Janes and Lowder⁴ found that the observed electron diffusion across the magnetic field lines is much greater than collisional diffusion processes could account for, and they attributed this anomalous diffusion to the transport resulting from low-frequency azimuthal waves.

The significant fluctuations measured in the near field lend support to the possible role that fluctuations may play in the anomalous cross-field diffusion of electrons from the external cathode to the exit plane of the thruster. We have estimated the cross-field transport that might occur from these relatively low-frequency disturbances within the framework of a drift-resistive instability driven by axial density gradients of characteristic scale, $L_{\nabla n} \approx O(10^{-2})$ m. Following Ref. 31, the dispersion of these waves is approximately

$$\omega \approx \omega_e^* (1 + i\alpha/4) (1 + k_{\perp}^2 \rho_s^2)^{-1}, \quad (3)$$

where $\omega_e^* = k_{\theta} k T_e / e B L_{\nabla n} \approx 4 \times 10^6$ rad/s is the characteristic drift wave frequency with $k_{\theta} \approx 50$ rad/m and $k_z = (k_{\perp}^2 - k_{\theta}^2)^{1/2} \approx 50$ rad/m, the azimuthal and axial component wave numbers (waves appear to propagate at about 45° forming the helix), and $\rho_s = c_i / \omega_{ci} \approx 0.15$ m, i.e., the ratio of the ion acoustic speed to the ion cyclotron frequency. The parameter α ($\approx 4 \times 10^{-3}$ in this case) is proportional to the growth rate of the drift wave instability,

$$\alpha \approx 4 \omega_e^* / \omega_s (1 + k_{\perp}^2 \rho_s^2)^2, \quad (4)$$

where $\omega_s \approx \omega_{ce} \omega_{ci} / \nu_e$ ($\approx 7 \times 10^5$ rad/s in our case) is the product of the electron and ion cyclotron frequencies and the inverse electron collision frequency taken to be the bounce frequency between the inner and outer magnetic poles ($\approx 10^7$ s⁻¹).

A quasilinear estimate can be made of the axial electron current in the near field from the measured fluctuation amplitudes in plasma potential, $\tilde{\phi} \approx 10$ V. From the predicted fluctuation amplitudes in both plasma density and electron velocity, we estimate

$$J_e \approx \frac{\alpha n_0 e^2 k_{\theta} k_{\perp}^2 \rho_s^2}{4kT_e B} \tilde{\phi}^2 \approx 10^2 \text{ A/m}^2 \quad (5)$$

with an exit plane area of $\sim 10^{-3}$ m². This corresponds to a current of about 0.1 A or roughly 10% of the discharge current. At this value, these low-frequency drift waves can certainly account for the current density in the very near field of these Hall discharges; however, we note that the frequency predicted by the dispersion equation above is about a factor of 3 and 4 lower than that seen in the experiments and that

the theory presented in Ref. 31 is for a noncurrent carrying plasma. The theory requires refinement to account for the relatively large current carried axially in the base (unperturbed) plasma and is the subject of future studies.

ACKNOWLEDGMENTS

This research was supported by the Air Force Office of Scientific Research with Dr. Mitat Birkan as program manager. A.W.S. acknowledges the support of the National Defense Science and Engineering Graduate Fellowship program.

- ¹W. Grossman, R. V. Hess, and H. A. Hassan, *AIAA J.* **6**, 1034 (1965).
- ²A. I. Morozov, A. Y. Kislov, and I. P. Zubkov, *JETP Lett.* **7**, 172 (1968).
- ³W. A. Hargus and M. A. Cappelli, *Appl. Phys. B: Lasers Opt.* **B72**, 961 (2001).
- ⁴G. S. Janes and R. S. Lowder, *Phys. Fluids* **9**, 1115 (1966).
- ⁵N. B. Meezan, W. A. Hargus, and M. A. Cappelli, *Phys. Rev. E* **63**, 026410 (2001).
- ⁶A. Lazurenko, T. D. de Wit, C. Cavoit, V. Krasnoselskikh, A. Bouchoule, and M. Dudeck, *Phys. Plasmas* **14**, 033504 (2007).
- ⁷D. Bohm, H. S. Burhop, and H. S. W. Massey, in *The Characteristics of Electrical Discharges in Magnetic Fields*, edited by A. Guthrie and R. K. Wakerling (McGraw-Hill, New York, 1949).
- ⁸A. I. Morozov and V. V. Savel'ev, *Plasma Phys. Rep.* **27**, 570 (2001).
- ⁹S. Barral, K. Makowski, Z. Peradzynski, N. Gascon, and M. Dudeck, *Phys. Plasmas* **10**, 4137 (2003).
- ¹⁰J. M. Fife, Ph.D. thesis, Massachusetts Institute of Technology, 1998.
- ¹¹G. J. M. Hagelaar, J. Bareilles, L. Garrigues, and J. P. Boeuf, *J. Appl. Phys.* **91**, 5592 (2002).
- ¹²B. E. Beal, A. D. Gallimore, and W. A. Hargus, *Phys. Plasmas* **12**, 123503 (2005).
- ¹³B. E. Beal, A. D. Gallimore, J. M. Haas, and W. A. Hargus, *J. Propul. Power* **20**, 985 (2004).
- ¹⁴W. A. Hargus and M. A. Cappelli, *J. Propul. Power* **18**, 159 (2002).
- ¹⁵A. Smirnov, Y. Raitses, and N. J. Fisch, *J. Appl. Phys.* **95**, 2283 (2004).
- ¹⁶A. Shirasaki and H. Tahara, *J. Appl. Phys.* **101**, 073307 (2007).
- ¹⁷L. Albarede, S. Mazouffre, A. Bouchoule, and M. Dudeck, *Phys. Plasmas* **13**, 063505 (2006).
- ¹⁸V. Hruba, J. Monheiser, B. Pote, P. Rostler, J. Kolencik, and C. Freeman, 30th Plasma Dynamics and Lasers Conference, Norfolk, VA, 1999.
- ¹⁹J. P. Boeuf and L. Garrigues, *J. Appl. Phys.* **84**, 3541 (1998).
- ²⁰E. Y. Choueiri, *Phys. Plasmas* **8**, 1411 (2001).
- ²¹J. M. Haas and A. D. Gallimore, *Phys. Plasmas* **8**, 652 (2001).
- ²²N. Hershkowitz, in *Plasma Diagnostics: Discharge Parameters and Chemistry*, edited by O. Auciello and D. L. Flamm (Academic, New York, 1989), Vol. 1.
- ²³W. A. Hargus, Ph.D. thesis, Stanford University, 2001.
- ²⁴R. F. Kemp and J. M. Sellen, *Rev. Sci. Instrum.* **37**, 455 (1966).
- ²⁵A. Navrotskii, *Metallurgist* **35**, 128 (1991).
- ²⁶L. Dorf, Y. Raitses, and N. J. Fisch, *Rev. Sci. Instrum.* **75**, 1255 (2004).
- ²⁷Y. Raitses, D. Staack, A. Smirnov, and N. J. Fisch, *Phys. Plasmas* **12**, 073507 (2005).
- ²⁸W. A. Hargus and B. Pote, 38th American Institute of Aeronautics and Astronautics/American Society of Mechanical Engineers/Society of Manufacturing Engineers/Society of Automotive Engineers/American Society for Engineering Education (AIAA/ASME/SME/SAE/ASEE) Joint Propulsion Conference, Indianapolis, IN, 2002.
- ²⁹W. A. Hargus and C. S. Charles, 44th American Institute of Aeronautics and Astronautics/American Society of Mechanical Engineers/Society of Manufacturing Engineers/Society of Automotive Engineers/American Society for Engineering Education (AIAA/ASME/SME/SAE/ASEE) Joint Propulsion Conference, Hartford, CT, 2008.
- ³⁰D. H. Manzella, 30th American Institute of Aeronautics and Astronautics/American Society of Mechanical Engineers/Society of Manufacturing Engineers/Society of Automotive Engineers/American Society for Engineering Education (AIAA/ASME/SME/SAE/ASEE) Joint Propulsion Conference, Indianapolis, IN, 1994.
- ³¹D. G. Swanson, in *Plasma Waves*, 2nd ed., edited by S. Cowley, P. Stott, and H. Wilhelmsson (Institute of Physics, University of Reading, Berkshire, 2003), pp. 308–310.